MIT Libraries | DSpace@MIT

MIT Open Access Articles

Real-Time MEG Source Localization Using Regional Clustering

Massachusetts Institute of Technology

CrossMark

ORIGINAL PAPER

Real-Time MEG Source Localization Using Regional Clustering

Christoph Dinh[1,2] · Daniel Strohmeier[2] · Martin Luessi[1] · Daniel Güllmar[3] ·
Daniel Baumgarten[2] · Jens Haueisen[2,4] · Matti S. Hämäläinen[1]

Abstract With its millisecond temporal resolution, Magnetoencephalography (MEG) is well suited for real-time monitoring of brain activity. Real-time feedback allows the adaption of the experiment to the subject's reaction and increases time efficiency by shortening acquisition and off-line analysis. Two formidable challenges exist in real-time analysis: the low signal-to-noise ratio (SNR) and the limited time available for computations. Since the low SNR reduces the number of distinguishable sources, we propose an approach which downsizes the source space based on a cortical atlas and allows to discern the sources in the presence of noise. Each cortical region is represented by a small set of dipoles, which is obtained by a clustering algorithm. Using this approach, we adapted dynamic statistical parametric mapping for real-time source localization. In terms of point spread and crosstalk between regions the proposed clustering technique performs better than selecting spatially evenly distributed dipoles. We conducted real-time source localization on MEG data from an auditory experiment. The results demonstrate that the proposed real-time method localizes sources reliably in the superior temporal gyrus. We conclude that real-time source estimation based on MEG is a feasible, useful addition to the standard on-line processing methods, and enables feedback based on neural activity during the measurements.

Keywords Magnetoencephalography · Real-time · Source localization · Minimum-norm estimates · K-means clustering · Brain atlas

✉ Christoph Dinh
chdinh@nmr.mgh.harvard.edu

1 Massachusetts General Hospital - Massachusetts Institute of Technology - Harvard Medical School, Athinoula A. Martinos Center for Biomedical Imaging, 149 13th St., Charlestown, MA 02129, USA

2 Institute of Biomedical Engineering and Informatics, Technische Universität Ilmenau, Gustav-Kirchhoff-Str. 2, 98693 Ilmenau, Germany

3 Medical Physics Group, Institute of Diagnostic and Interventional Radiology, Friedrich-Schiller-Universität Jena, Philosophenweg 3, 07743 Jena, Germany

4 Biomagnetic Center, Department of Neurology, Friedrich-Schiller-Universität Jena, Erlanger Allee 101, 07743 Jena, Germany

Introduction

Magnetoencephalography (MEG) is a noninvasive technique to investigate neural activity with a high temporal resolution (Hamalainen et al. 1993). Source estimation methods, such as minimum-norm estimation (MNE), can be applied to map the sensor space measures to sources in the brain. Recently, methodological advances have made real-time MEG source estimation possible (Sudre et al. 2011). This approach can be used to better understand brain function, to identify mental states (Jones et al. 2010; Ziegler et al. 2010), and to create more effective brain-computer interface (BCI) systems (Soekadar et al. 2011; Besserve et al. 2011). Monitoring the activity at the source level enables, for example, the adaption of the experiment (feedback), real-time adjustment of neuro implants, and real-time monitoring of drug effects Michel et al. (1995).

Two major challenges in real-time source localization are the low signal-to-noise ratio (SNR) of single-trial as

well as moving-average measurements and the limited time available for computations. Chowdhury et al. (2013) recently published a data-driven method for parceling the cortical surface based on a pre-source localization, which determines seed points to create parcels for each measurement setup. This set of functionally homogeneous active areas results in a smaller gain matrix and as a result the inverse problem becomes better conditioned.

In this work, we present a novel model-driven clustering method for real-time source localization to handle the low SNR and to reduce the computational cost. Our method is based on two assumptions. First, it is assumed that the neural activity is spatially smooth and can be organized into cortical parcels (Chowdhury et al. 2013; Dinh et al. 2012). This spatial smoothness justifies that a whole region can be activated in the same quantity as a region's representative dipole. Second, it is assumed that a low SNR reduces the number of distinguishable sources (Supek and Aine 1993; Tarkiainen et al. 2003). These assumptions lead to different possibilities to obtain a reduced inverse operator. Based on the comparison of these approaches, we propose to cluster the dense gain matrix (Dinh et al. 2012) based on a cortical atlas (Destrieux et al. 2010) into a reduced matrix which maps neural activity to parcellated cortical regions.

To realize complex real-time processing chains requires a highly generic and scalable software framework. For this purpose we utilize our in-house real-time acquisition and processing solution MNE-X, which is designed for the acquisition and processing of real-time data streams from multiple sensors. MNE-X is part of our EEG/MEG data processing software MNE-CPP which we made recently available (Dinh et al. 2013) under an open source license. The software package can be downloaded at: https://github.com/mne-tools/mne-cpp [1]

Methods

Gain Matrix Reduction

The relationship of MEG signals and their sources is

$$y = Gq + \epsilon, \tag{1}$$

where the vector y contains the signals measured at the sensors, G is the gain matrix, q contains the amplitudes of dipole sources, and ϵ is the noise. The column vector triplet of G mapping the dipole triplet at the rth (cortical) site to the sensors will be denoted by g_r. In our approach, the dipoles were approximately evenly distributed on the white matter surface.

Many source estimates can be expressed as the solution of the minimization problem

$$\hat{q} = \arg \min_q (\|y - Gq\| + f(q)), \tag{2}$$

where the first term expresses a (weighted) norm of the differences between the measured signals and those predicted by the model while $f(q)$ incorporates the a priori assumptions. One popular solution is the minimum-norm estimate (MNE) (Hamalainen and Ilmoniemi 1994). In this approach, f(q) is the squared L_2-norm of the currents, weighted by a regularization parameter λ^2, and the solution is obtained by multiplying the data with the linear inverse operator:

$$\hat{q} = My, \tag{3}$$

where

$$M = G^T (GG^T + \lambda^2 C)^{-1}. \tag{4}$$

In the above, C is the noise covariance matrix and λ^2 is the regularization parameter adjusting the relative weight of the two terms in Eq. 2.

One way to set the regularization parameter is to relate it to the SNR of the whitened data. This approach is described in detail by Lin et al. (2006).

MNE is fast to compute, it is thus potentially useful for real-time source localization. The main goal of this work was to improve the capability of MNE to handle low SNRs and to further accelerate the computation for real-time source localization.

To achieve these goals, we represent regional cortical activity by a small number of dipoles. We thus preserved dipoles which could still be distinguished in the presence of low SNRs. At the same time, we reduced the computational complexity. To justify the reduction, it had to be assumed that neural activity is spatially smooth and can be organized into parcels, representing anatomical units, which in many cases have a functional meaning. It was further assumed that nearby dipoles produce very similar MEG signal patterns.

We considered four methods to reduce the gain matrix. The most obvious method was a selection of a smaller set of spatially evenly distributed dipoles, which reduces the computational effort and improves the condition of the inverse problem at the same time. We compared this selection method to three different clustering methods, which are based on clustering either a high-resolution gain matrix G or directly the inverse operator M. To our knowledge, the clustering approach has not been used in real-time source localization before.

Clustering Methods

By reducing the gain matrix through clustering, we aimed at the region-wise calculation of the most representative

---

[1] At this point we want to emphasis that everybody is very welcome to contribute to and to participate of the further development of this package.
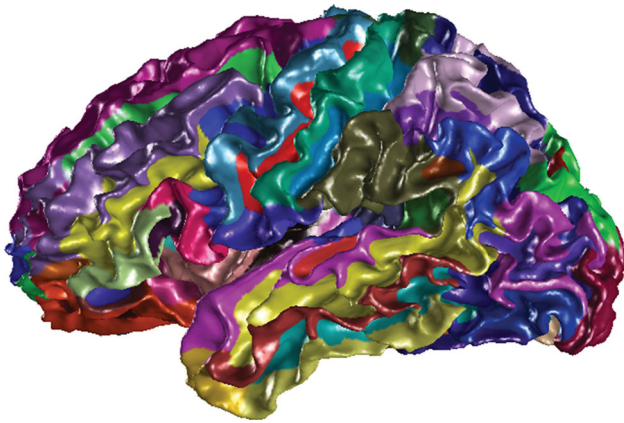
Fig. 1 The Destrieux's brain atlas (Destrieux et al. 2010), which divides the cortex into 74 anatomical, often related to functional, units in each hemisphere

dipoles instead of the arbitrary selection of dipoles which are not ensured to be representative. In order to preserve the spatial and anatomical relations when clustering the gain matrix, an anatomical brain atlas was used to divide the brain into several anatomical units, which often have a functional meaning, see Fig. 1.

We employed three different clustering methods: (I) a clustering based on the gain matrix G, (II) a combined clustering based on G and the inverse operator M, and (III) a clustering directly based on the inverse operator M.

Method I

According to the atlas, the gain matrix G can be divided into a set of s sub-gain matrices:

$$G = \{G_1, \ldots, G_s\}. \tag{5}$$

Dipoles belonging to these region-related subsets G_i were clustered into k_i clusters using the k-means algorithm (Lloyd 1982).

Prior to clustering, we whitened the gain matrix with the spatial noise covariance matrix C estimated from the baselines of evoked response data:

$$\widetilde{G} = C^{-1/2}G. \tag{6}$$

The whitening takes into account different units of measure (planar gradiometers vs. magnetometers in the Elekta Neuromag® VectorView™) and different noise levels in the channels. After whitening, the gain vectors were clustered region by region:

$$K(\widetilde{G_i}) = \sum_{r=1}^{n_{\widetilde{G_i}}/k_i} \min_{j \in 1 \ldots k_i} \left\| \widetilde{g}_r - \mu_j \right\|_p \quad (p = 1, 2). \tag{7}$$

The aim of k-means $K(\widetilde{G_i})$ was to calculate the centroid μ_j, which was assumed to be a representative dipole of a

cluster, which consists of n_{G_i} dipoles belonging to one or a part of one region. The L_1-norm ($p = 1$) and the L_2-norm ($p = 2$) were used and compared as two separate distance measures within the k-means algorithm. All k-means cluster indices forming separate dipole centroids can be concatenated to one cluster operator $D_{\widetilde{G}}$, which clusters the original gain matrix G at once:

$$G^* = GD_{\widetilde{G}} \tag{8}$$

and the corresponding inverse operator is:

$$M_D = D_{\widetilde{G}}^T G^T (GD_{\widetilde{G}} D_{\widetilde{G}}^T G^T + \lambda^2 C)^{-1}. \tag{9}$$

In the following, we refer to this method as I_{L1} and I_{L2}, depending on the norm employed in clustering, see Table 1.

The number of clusters k_i for each region depends on the number of dipoles n_{G_i} in each region. It is determined by:

$$k_i = \min\left\{ k \in \mathbb{Z} \,|\, k_i = \lceil \frac{n_{G_i}}{z} \rceil \right\}, \tag{10}$$

where the cluster size z represents a reduction constant. It specifies the number of dipoles clustered to one centroid. The optimal constant z is calculated with the help of the condition number κ of the clustered gain matrix $G^*(z)$ (Sect. 3.1):

$$\kappa(G^*(z)) = \left| \frac{\sigma_{\max}(G^*(z))}{\sigma_{\min}(G^*(z))} \right|, \tag{11}$$

where $\sigma_{\max}$ and $\sigma_{\min}$ refer to the maximal or minimal singular value of the clustered gain matrix G^*, respectively. A lower condition number κ represents better conditioned data. Different cluster sizes z and k-means distance measures yield different condition numbers κ.

The optimal reduction constant z corresponds to the minimal condition number:

$$z_{opt} = \arg\min_{z \in \mathbb{Z}}(\kappa(G^*(z))). \tag{12}$$

Method II

In this approach, we applied the cluster indices $D_{\widetilde{G}}$ (Eq. 6) of Method I to M, thus effectively clustering the source estimate values based on the full gain matrix:

$$D_{\widetilde{G}}^T M = D_{\widetilde{G}}^T G^T (GG^T + \lambda^2 C)^{-1}. \tag{13}$$

This left the inner term of Eq. 9 untouched:

$$GD_{\widetilde{G}} D_{\widetilde{G}}^T G^T. \tag{14}$$

In analogy with method I, this method is referred to as II_{L1} and II_{L2} depending on whether the L_1- or L_2-norm is used in clustering, see Table 1.

Table 1 Overview of different inverse operators evaluated

	Description	Complexity
L₁ based K-Means		
I_{L1}	M based on G^*	$\mathcal{O}(n^*m^2)$
II_{L1}	Cluster M, derive cluster indeces of $\widetilde{G}$	$\mathcal{O}(nm^2 + nmn^*)$
III_{L1}	Cluster M	$\mathcal{O}(nm^2 + nmn^* + \sum_{i=1}^{s} n_{G_i}^{mk_i+1} \log n_{G_i})$
L₂ based K-Means		
I_{L2}	K-means is based on L_2- instead of L_1- norm.	
II_{L2}		
III_{L2}		
No Clustering		
IV	The number of selected dipoles is the same as the number of centroids in methods I–III	$\mathcal{O}(n^*m^2)$

An estimation for the real-time computational burden is given by the complexity

n^* number of cluster dipoles, n number of dipoles, m number of MEG sensors, k_i number of clusters of region i, n_{G_i} number of dipoles of region i

Method III

In this method the clustering was based on the source waveforms, i.e., the unclustered inverse operator M, instead of the gain matrix G and we thus obtained the inverse operator

$$D_{M^T}^T M = D_{M^T}^T G^T (GG^T + \lambda^2 C)^{-1}. \tag{15}$$

In consequence the source space was taken as ground truth, no matter how sensitive the sensors were to a particular dipole location.

Method IV

In method IV (the selection method), the reduced gain matrix G^* was created by selecting a subset of equally distributed dipoles of the original gain matrix G. The selected dipoles then acted as representations of the anatomical units each of them belongs to (Fig. 1). This helped to interpret the result even though the source space was highly decimated. Furthermore the result was comparable to the clustering method described in the previous paragraph. In the following, we refer to the selection method by IV, see Table 1.

Comparison

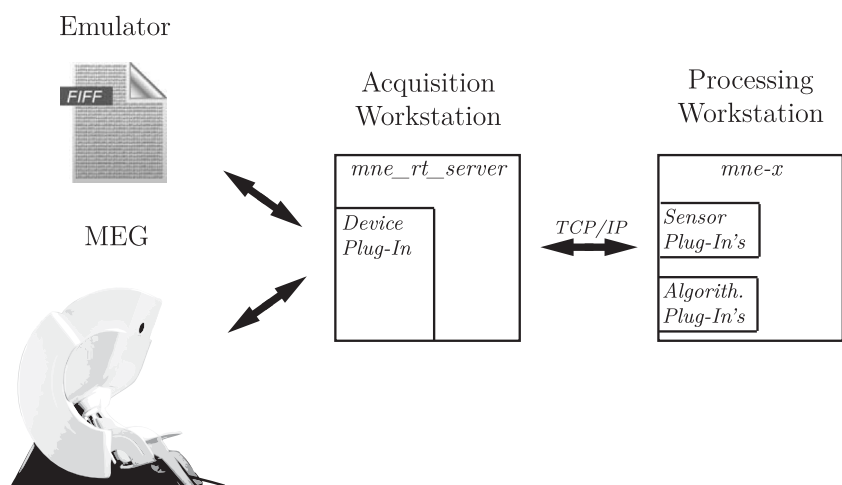The different methods were evaluated by comparing point spread and crosstalk computed from the resolution matrix

$$R = MG. \tag{16}$$

The point spread is a measure on how focal the source estimation is, i.e., how strong neighbored sources are activated together with the actual active source. On the other hand, the crosstalk is a measure for the activation across the whole source space including non-neighbored sources.

The columns of R describe the point spread across regions when a given source in the dense source grid is active. The relative average point spread ψ was calculated by combining all values belonging to one region, i.e., source activities of one region, divided by the activities of all regions:

$$\psi = 1 - \frac{1}{\text{card}(\forall j \in v_k)} \frac{\sum_{o \in v_k} \sum_{j \in v_k} R_{oj}}{\sum_{j \in v_k} \left(\sum_{o \in v_k} R_{oj} + \sum_{o \notin v_k} R_{oj} \right)}. \tag{17}$$

Fig. 2 Acquisition chain: Data were collected with *mne_rt_server* directly from the medical or emulated medical device. Multiple clients, e.g., MNE-X, can be connected to the real-time server

Emulator

FIFF

MEG

Acquisition Workstation

mne_rt_server

Device Plug-In

TCP/IP

Processing Workstation

mne-x

Sensor Plug-In's

Algorith. Plug-In's

The current region is referred to as v_k. A lower value ψ refers to a decreased point spread and is therefore better.

The relative crosstalk χ, caused by the activity of one region towards all other vertices can be found among the rows of R. Within one row, the vertices belonging to one cluster v_k are put into relation to all vertices.

$$\chi = \frac{\alpha}{\alpha + \beta}$$
$$\alpha = \frac{1}{\text{card}(\ \forall j \notin v_k)} \sum_{j \notin v_k} R_{kj}^2 \qquad (18)$$
$$\beta = \frac{1}{\text{card}(\forall j \in v_k)} \sum_{j \in v_k} R_{kj}^2$$

A lower relative crosstalk has to be preferred.

The Real-Time Processing Chain

The real-time processing chain was realized with two applications of the MNE-CPP software package Dinh et al. (2013), see Sect. 1 and Fig. 2.

The first application is *mne_rt_server*, with a plug-in based architecture to realize several different medical device connectors. This application converts the measured data to a standardized real-time fiff data stream. Fiff is the file format used by Elekta Neuromag® to store acquired data. The *mne_rt_server* fiff data stream can be accessed over a TCP/IP connection.

The second application is *MNE-X*, written in Qt C++ (Digia Plc 1991–2014), to acquire and process the data. It provides the functionality to control the MEG acquisition, to record the acquired data, and to process them in real-time. It has a generic plug-in architecture which can easily be extended. The real-time source localization is realized as an algorithm plug-in, see Fig. 3.

For real-time localization of evoked responses we employed a moving average of N_e responses. We assumed that the fraction of time occupied by the evoked response is small enough so that we could use the raw data directly to estimate the noise covariance matrix C.
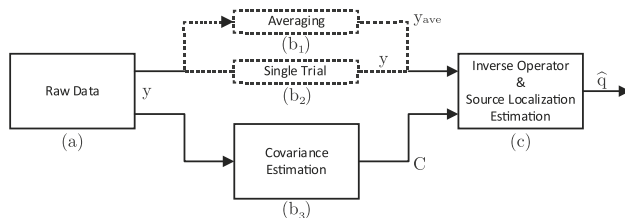

Fig. 3 The source localization processing chain; (*a*) acquired data stream; independent averaging (b_1) or single-trial (b_2) and covariance C estimation (b_3); (*c*) Source localization which estimates sources $\hat{q}$ using the averaged data y_{ave} and the continuously updated inverse operator M.

A new noise covariance matrix C was calculated every n_C samples and the inverse operator was updated accordingly.

We also computed a noise-normalized estimate (dynamic statistical parametric mapping—dSPM) (Dale et al. 2000) to reduce the location bias of the estimates and to decrease the dependency of the point-spread function on the source location.

Data Acquisition

As described in Sect. 2.2 *mne_rt_server* provides several plug-ins, including the Elekta Neuromag® MEG VectorView™ system plug-in and the MEG system emulator plug-in. Since there is no difference in the processing pipeline between having an actual subject inside the MEG room or using a previously recorded raw file as a subject emulation, we used the emulation plug-in to evaluate the developed algorithm and to find the optimal adjustments. The emulation configuration, *mne_rt_server* together with the emulation plug-in run on the Neuromag acquisition workstation, allows the emulation of the study as it would be carried out in real-time. The emulated data had a sampling frequency of 1250 Hz.

Data of five subjects of the MIND multi-site MEG study (Weisend et al. 2007; Ou et al. 2007) using two different auditory recordings for each subject were used to evaluate the four reduction methods. In the auditory task of this study, three pure tones of different frequencies (500, 2000, and 4000 Hz) were presented to obtain a tonotopic map. The tones were randomly presented with an average inter-stimulus interval of 1157 ± 891 ms. The stimuli were delivered to the subject's ear canal using sound transducers connected with plastic tubing to ergonomically designed earplugs. An attenuator was used to adjust the intensity of the tones. The hearing thresholds were determined individually for each subject before the session. The figures in the following sections were created using one data set of this study.

Subsequently, we conducted a measurement with the Elekta Neuromag® MEG system plug-in to confirm the real-time performance.

Wehner et al. (2008) described the influence of head movement of children in MEG on source localization. They used an Elekta Neuromag® MEG VectorView™ system as well. It turned out that source localization is relatively robust to head movement. It appeared that the frontal cortex is most prone to localization errors, with a worst case mean error of 12 mm. Localizations within the auditory cortex are more robust towards head movement. Therefore, we did not include motion correction in the data processing.

The anatomical model was based on individual MRI data collected with a Siemens Magnetom® Avanto 1.5 T

MR scanner. Four different sequences were acquired: two MPRAGE sequences with a receiver band width of 240 and 650, and two FLASH sequences with a flip angle of 5 and 30 °. The two MPRAGE sequences were used to reconstruct the motion corrected anatomical structures including the brain atlas which was performed with FreeSurfer (Fischl 2012). The volume conductor modeling was done with the MNE suite (Gramfort et al. 2013) using the FLASH sequences creating a three layer (outer skin; outer skull; inner skull) boundary element model. The gain matrix was calculated for approximately 7500 uniformly distributed dipoles on the white matter surface.

Evaluation

We determined the best performing selection / clustering method by comparing point spread and crosstalk (Eqs. 17, 18). These two measures were analyzed using nonparametric statistics, since the underlying distribution was not known. Friedman's (1937) test was used to determine whether the distribution underlying the crosstalk and point spread results are significantly different. In a next step the Wilcoxon–Mann–Whitney test (Wilcoxon 1945; Mann and Whitney 1947) was applied to unveil significant differences between each single method. To counteract the multiple comparison problem we employed the Bonferroni correction, which reduces the test threshold p_t given by the significance level p by the number of pairwise comparisons n_c:

$$p_t = \frac{p}{n_c}. \tag{19}$$

We took the condition as a measure for the robustness of the inverse problem towards noisy data, i.e., the inverse problem using a better conditioned gain matrix (Eq. 11) is less influenced by low SNRs (Eichardt et al. 2012). The optimal cluster size was found by evaluating the condition of different sized gain matrices, see Eq. 11. Moreover, the condition was taken as a figure of merit to reveal whether the L_1- or L_2-norm performs better in clustering. The influence of clustering on the distribution of the dipole sensitivity was analyzed subsequently. The cluster centers of G^* were mapped to the location of the most similar dipole of the original gain matrix G to obtain their coordinates. We also evaluated the source localization precision of the method with the lowest point spread and crosstalk. A dipole fit based on the MIND data (see Sect. 2.3) was calculated as reference localization. The dipole fit was applied to the baseline (-100 to 0 ms pre-stimulus interval) corrected, 1–40 Hz band-pass filtered, averaged data, which contained all available trials of the left auditory evoked 500 Hz stimulus fields. The dipole fitting was performed in the Elekta Neuromag® Xfit software.

The localized ipsi- and contralateral dipoles were mapped to their closest corresponding Destrieux's brain region, see Fig. 1, which were taken as reference regions. In the next step, we calculated MNE employing the reduced gain matrix G^* and $N_e = 1, 2, 4, 10,$ and 20. Each localization was repeated 31 times using different random selections of trials. The smallest distance between the reference dipole and the most active localized region was taken as localization error, i.e., the root-mean-square error was calculated between the reference dipole and the vertex of the respective region which was closest to the reference dipole. The most active region was determined based on the source activity of a single time point (0.12 s) or the average of the source samples between 0.116–0.124, 0.113–0.127 ms or 0.11–0.13 ms. The average of source samples was calculated to smooth the estimated source activity, which was highly transient caused by noise. The error measure was determined for each hemisphere.

Finally, we verified the real-time performance using the Elekta Neuromag® MEG VectorView™ system. The overall fixed delay t_Δ, caused by the processing chain was calculated based on the buffer sizes n_{buf} and the given sampling rate f_s:

$$t_\Delta = \frac{n_{\text{buf}}}{2} / f_s. \tag{20}$$

Results

Gain Matrix Reduction

Crosstalk and point spread (Eq. 16) were computed to determine the best selection / cluster method among those listed in Table 1. The results for a fixed number of approximately 416 centroids ($z = 20$, see cluster size investigation, next paragraph) over all subject recordings are shown in Figs. 4 and 7, representing histograms of the respective parameter in vertical direction. Friedman's test on the crosstalk medians (Fig. 5) of each recording showed with $p = 1.3495 \times 10^{-6}$ a significant difference among the methods given a significance level of $p = 0.05$. The method-wise comparison of the crosstalk medians using the Wilcoxon-Mann-Whitney test and the Bonferroni correction showed that the medians of the selection method (IV) and the original dense gain matrix were significantly different to the other methods' medians (Table 2). The selection method (IV) and the original dense gain matrix had the highest crosstalk across all subjects whereas the cluster based reduction methods (I–III) had similar low crosstalk values (Fig. 4).

In accordance with the crosstalk analysis we firstly analyzed the point spread (Fig. 6) with Friedman's test

Fig. 4 Relative crosstalk distribution over all subjects and measurements using different methods (Table 1) as well as the result of the original dense gain matrix. The violin plot shows a symmetric histogram of atlas regions. The length of the interval *bars* indicates the number of contained regions/ vertices. Mean values are indicated by *red bars* (Color figure online)
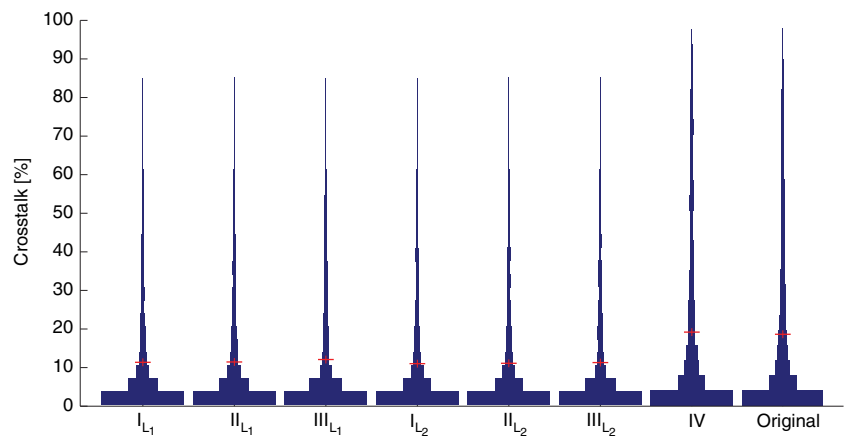

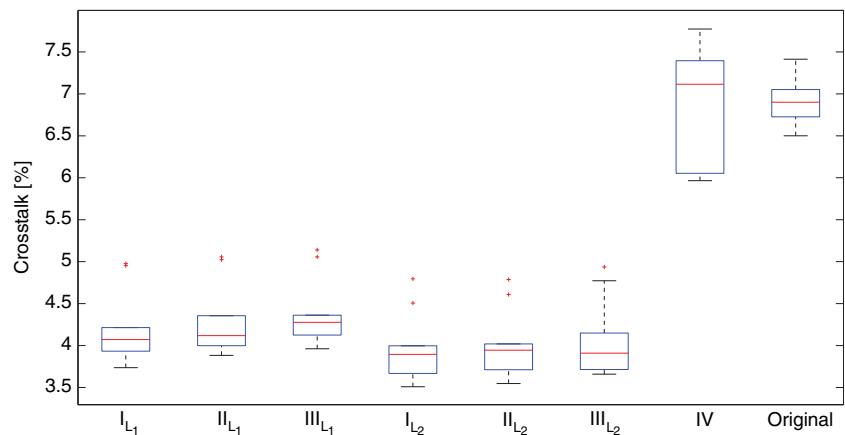**Fig. 5** Distribution of methods' crosstalk medians over all subjects and measurements

Table 2 Method-wise Wilcoxon–Mann–Whitney test on the crosstalk given a $p = 0.05$ significance level

	I_{L_1}	II_{L_1}	III_{L_1}	I_{L_2}	II_{L_2}	III_{L_2}	IV	Original
I_{L_1}	*1.0*	*0.4727*	*0.1212*	*0.0890*	*0.2123*	*0.2413*	**0.0002**	**0.0002**
II_{L_1}		*1.0*	*0.3447*	*0.0376*	*0.0539*	*0.0890*	**0.0002**	**0.0002**
III_{L_1}			*1.0*	*0.0140*	*0.0257*	*0.0376*	**0.0002**	**0.0002**
I_{L_2}				*1.0*	*0.7913*	*0.5708*	**0.0002**	**0.0002**
II_{L_2}					*1.0*	*0.7913*	**0.0002**	**0.0002**
III_{L_2}						*1.0*	**0.0002**	**0.0002**
IV							*1.0*	*0.8501*
Original								*1.0*

The Bonferroni correction reduces the test threshold by $n_c = 28$, which in consequence rejects the null hypothesis of equal medians for values smaller than $p_t = 0.0018$—italic: equal medians; bold: different medians. It can be seen that the selection method and original full gain matrix are significantly different to the proposed cluster methods. Whereas the crosstalk of the selection method (IV) and the original full gain matrix are the same

which revealed a significant difference of $p = 5.7442 \times 10^{-9}$ between the method's point spread median distributions given a significance level of $p = 0.05$. In the next step we also calculated the method-wise median comparison using the Wilcoxon-Mann-Whitney test in connection with a Bonferroni correction. The results showed that clustering the inverse operator (method III_{L_1}) and the original dense

gain matrix were significantly different across all subjects, see Table 3. The original dense gain matrix showed the highest point spread followed by method III_{L_1} whereas the other methods performed similarly well (Fig. 7).

Since the methods I_{L_1} and I_{L_2} had the lowest computational costs, see Table 1, an improvement in crosstalk of about 10% compared to method (IV), see Fig. 4, and the

Table 3 Method-wise Wilcoxon-Mann-Whitney test on the point spread given a $p = 0.05$ significance level

	I_{L_1}	II_{L_1}	III_{L_1}	I_{L_2}	II_{L_2}	III_{L_2}	IV	Original
I_{L_1}	*1.0*	*0.2413*	**0.0003**	*0.5205*	*0.4727*	*0.0539*	*0.1041*	**0.0002**
II_{L_1}		*1.0*	**0.0004**	*0.3075*	*0.2413*	*0.1620*	*0.3447*	**0.0002**
III_{L_1}			*1.0*	**0.0003**	**0.0003**	**0.0008**	*0.0091*	**0.0002**
I_{L_2}				*1.0*	*0.5205*	*0.0376*	*0.0539*	**0.0002**
II_{L_2}					*1.0*	*0.0312*	*0.0890*	**0.0002**
III_{L_2}						*1.0*	*0.7337*	**0.0002**
IV							*1.0*	**0.0002**
Original								*1.0*

We applied the same Bonferroni correction as in the test on the crosstalk, which as a result also rejects the null hypothesis of equal medians for values smaller than $p_t = 0.0018$—italic: equal medians; bold: different medians. It can be seen that method III_{L_1} and the original gain matrix have significantly different point spreads compared to the other proposed cluster methods

Fig. 6 Distribution of method's point spread medians over all subjects and measurements
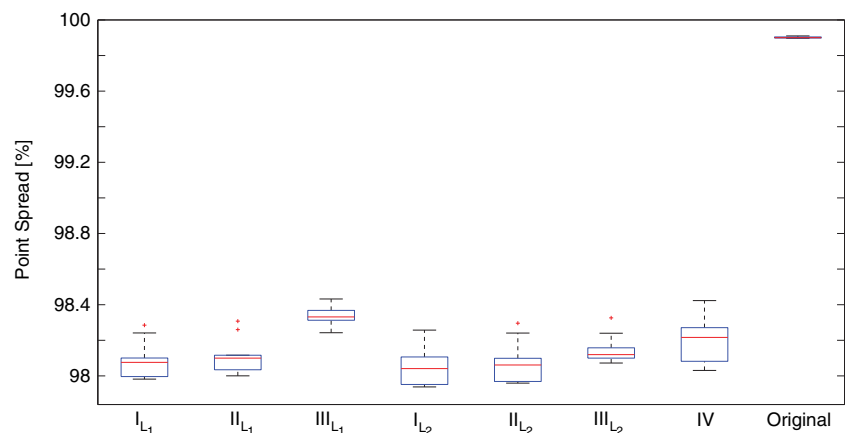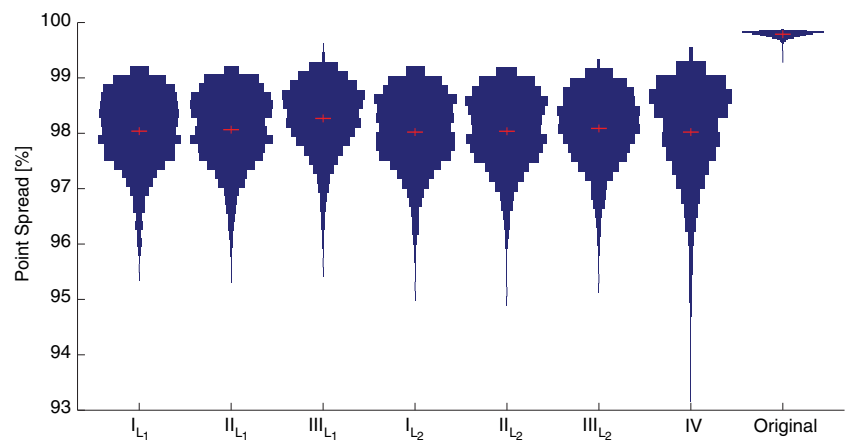

Fig. 7 Relative point spread over all subjects and measurements of different selection / cluster paradigms (Table 1). The violin plot shows a symmetric histogram of dipoles of regions. The length of the interval *bars* indicates the number of contained dipoles. Mean values are indicated by *red bars* (Color figure online)

point spread of method I_{L_1} was as good as others, we decided to choose method I_{L_1} as the best performing method.

In the above we used a cluster size which resulted in a reduced gain matrix containing approximately 416 dipoles. In the following, we show how we determined the optimal number of clusters. The best cluster size z was determined using the condition number κ (Eq. 11) as a figure of merit. Figure 8 illustrates that the condition number has at the beginning a large descent with increasing cluster sizes. This changes at a certain point back into a small increase

Fig. 8 Cluster size z and corresponding condition number κ. The smallest, meaning the optimal, condition number can be found for a cluster size containing about 11 dipoles. The applied k-means clustering uses a L_1-norm distance measure
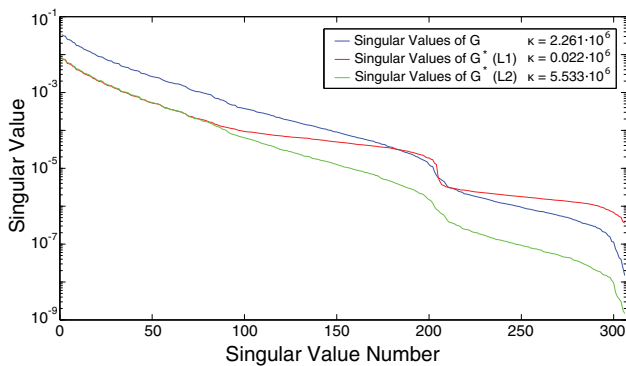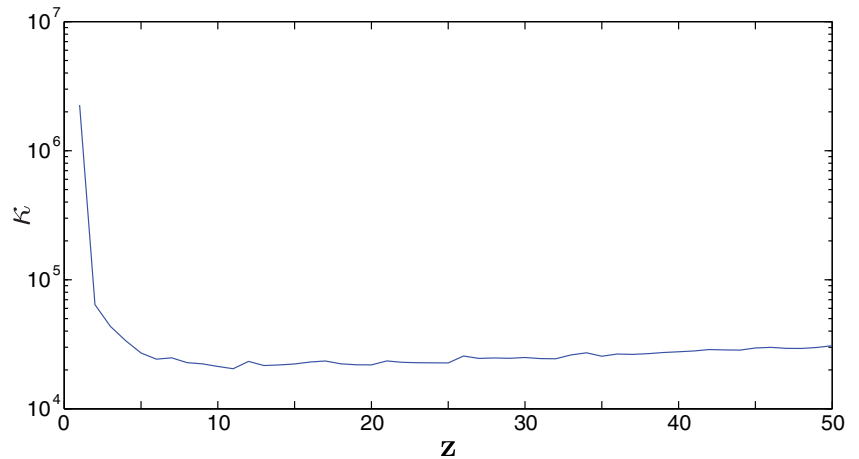
Fig. 9 Singular values of the full gain matrix G and the clustered (L_1 & L_2) gain matrices G^*. The singular values were used to determine the condition of the gain matrices
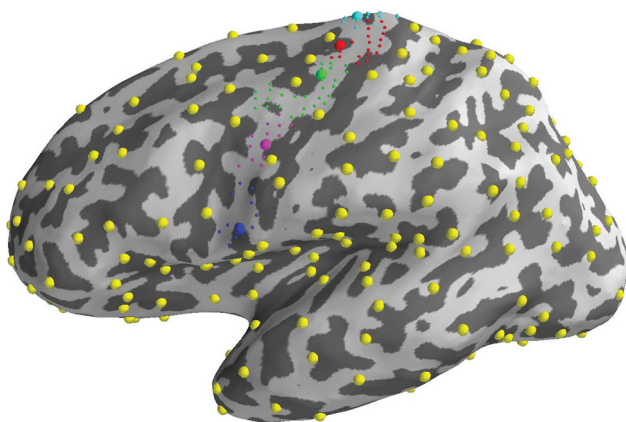
Fig. 10 Cluster dipoles (*large dots*) mapped to the closest dipole of the original gain matrix (*small dots*; only shown for the precentral gyrus). Mapped centroids of the precentral gyrus are colored differently, referring to the original dipoles (*small dots*) forming one centroid. (*Color codes* do not correspond to the atlas of Fig. 1)
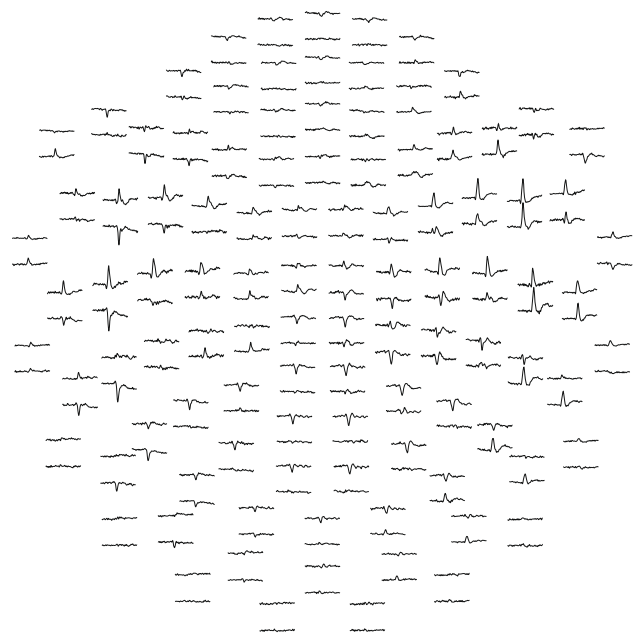
Fig. 11 Topographic plot for a Elekta Neuromag® MEG VectorView™ sensor configuration of the reference auditory evoked field. Data were baseline corrected and band-pass filtered

with larger cluster sizes. We empirically chose a cluster size z of 20, which seemed to be a good trade-off between a low condition number and a small clustered gain matrix for

an accelerated computation. This value reduced our gain matrix G containing approximately 7500 dipoles to a gain matrix G^* containing approximately 416 dipoles.

Figure 9 visualizes the singular values of the full gain matrix G and the clustered gain matrices G^* using the L_1- and the L_2-norm. The k-means clustering with the L_1-norm resulted in an improved condition whereas it decreased with the L_2-norm. The L_1-norm clustered gain matrix G^* had fewer dipoles revealing a stronger separation from each other compared to the original gain matrix G.

The mapping of the cluster centers of G^* to the closest dipole of the original gain matrix G allowed to obtain their coordinates. The distribution of these dipoles is illustrated

T = 0.122 s
r = [-52.4 mm; 12.8 mm; 67.5 mm]
gof = 90.3 %

T = 0.119 s
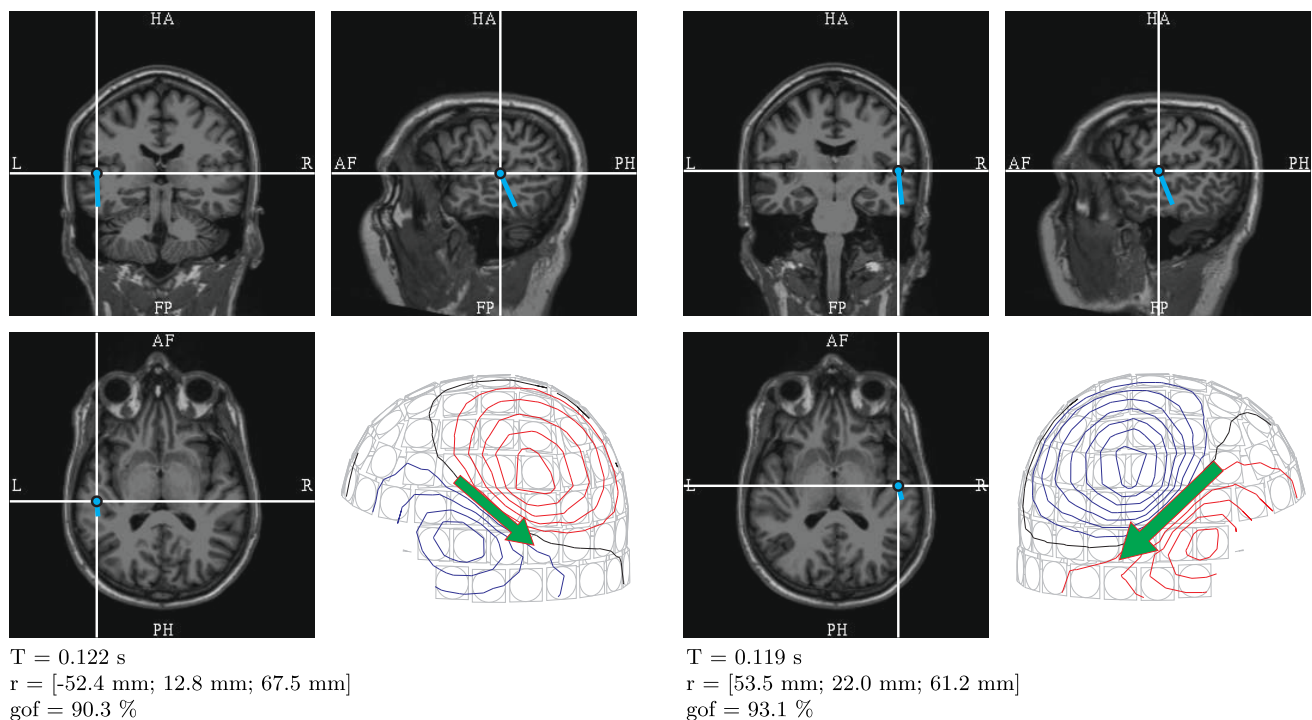r = [53.5 mm; 22.0 mm; 61.2 mm]
gof = 93.1 %

Fig. 12 The dipole fit, which was used as reference source localization. The dipole fit was created with the Elekta Neuromag® *Xfit* source localization toolbox. *T* - post stimulus time; *r* - location in the head coordinate system; *gof* - goodness-of-fit

in Fig. 10. It can be seen that the distribution almost uniformly covers the whole brain. The average values of the sensitivities in the original gain matrix G were $-0.29 \pm 30.59\ muT/Am$ for the gradiometers and $-0.04 \pm 44.67\ \mu T/Am^2$ for the magnetometers. The mapping of the centroids of G^* caused a deviation of $-0.06 \pm 5.97\ \mu T/Am$ for the gradiometers and $-0.05 \pm 5.26\ \mu T/Am^2$ for the magnetometers. Since this difference is relatively high, the centroids were used to construct G^* instead of the closest dipoles of G.

Noise Covariance Estimation

The noise covariance matrix was estimated in real-time and was used to calculate a new inverse operator M, which was therefore adapted to the present noise. The ergodicity was taken as description to determine the number of samples for a valid estimation of the noise covariance matrix.

The target ergodicity value change of less than 5% was reached when an interval of 4 s was used. Within our measurements we applied a sampling frequency of 1250 Hz, which resulted in a new covariance matrix estimation every 5000 samples. The data segments did not overlap.

Source Localization

First, the reference localization data were created by averaging all available 99 left ear auditory stimulus responses of one exemplary subject, which were subsequently baseline corrected and band-pass filtered, as described in Sect. 2.4. The reference data is shown in a topographical layout in Fig. 11.

A dipole fit for each hemisphere was calculated as reference localization, see Sect. 2.4. The results are shown in Fig. 12.

The reference dipoles were then mapped to the closest atlas region in both hemispheres. The obtained reference regions refer to the *superior temporal sulcus* for the ipsi and *anterior transverse temporal gyrus (of Heschl)* for the contra lateral hemisphere.

Method I_{L_1}, using MNE (see Table 1), was now computed in the clustered source space. The localization error between reference and localized region was calculated as described in Sect. 2.4. The results are shown in Fig. 13.

The results for a sample-wise reconstruction were lowest for localizations based on 10–20 averages. For the following analysis we decided to consider averages including 10 epochs, which allowed to have a good trade-off between the aim to monitor changes in the activity and the necessary noise reduction for a higher localization precision. One localization result based on the average of 10 randomly selected epochs from the example data set is shown in Fig. 14, which shows the waveforms of the sources over time as well as the mapped source activity at the N100 of the left auditory stimulus.

Finally, we verified the real-time delays with the Elekta Neuromag® VectorView 306™ MEG device. We were able
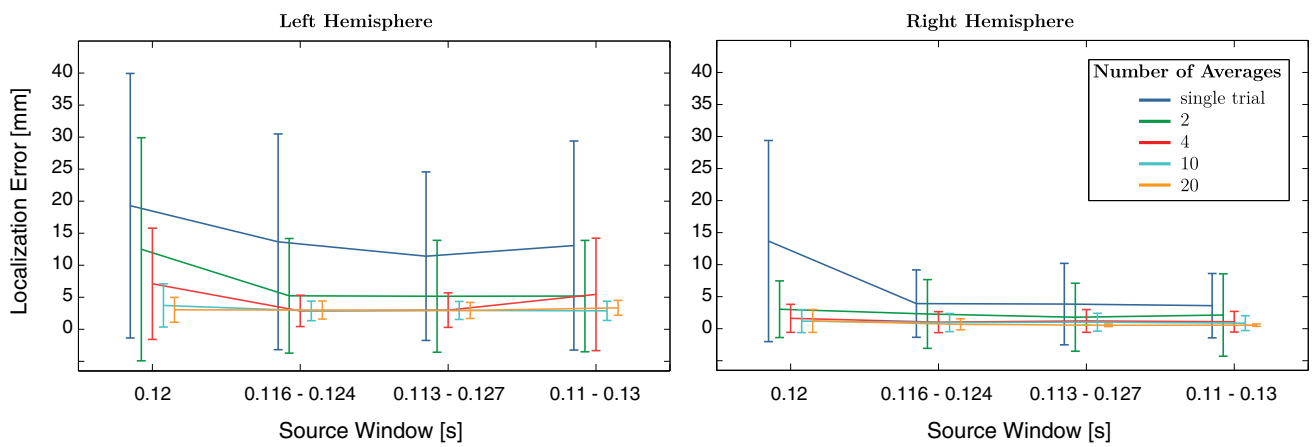
Fig. 13 This Figure shows the localization error between reference and localized most active region. The most active region for each hemisphere was determined based on the source activity of one time point (0.12 s) or the average of source samples within an interval (0.116–0.124 s; 0.113–0.127 s; or 0.11–0.13 s).
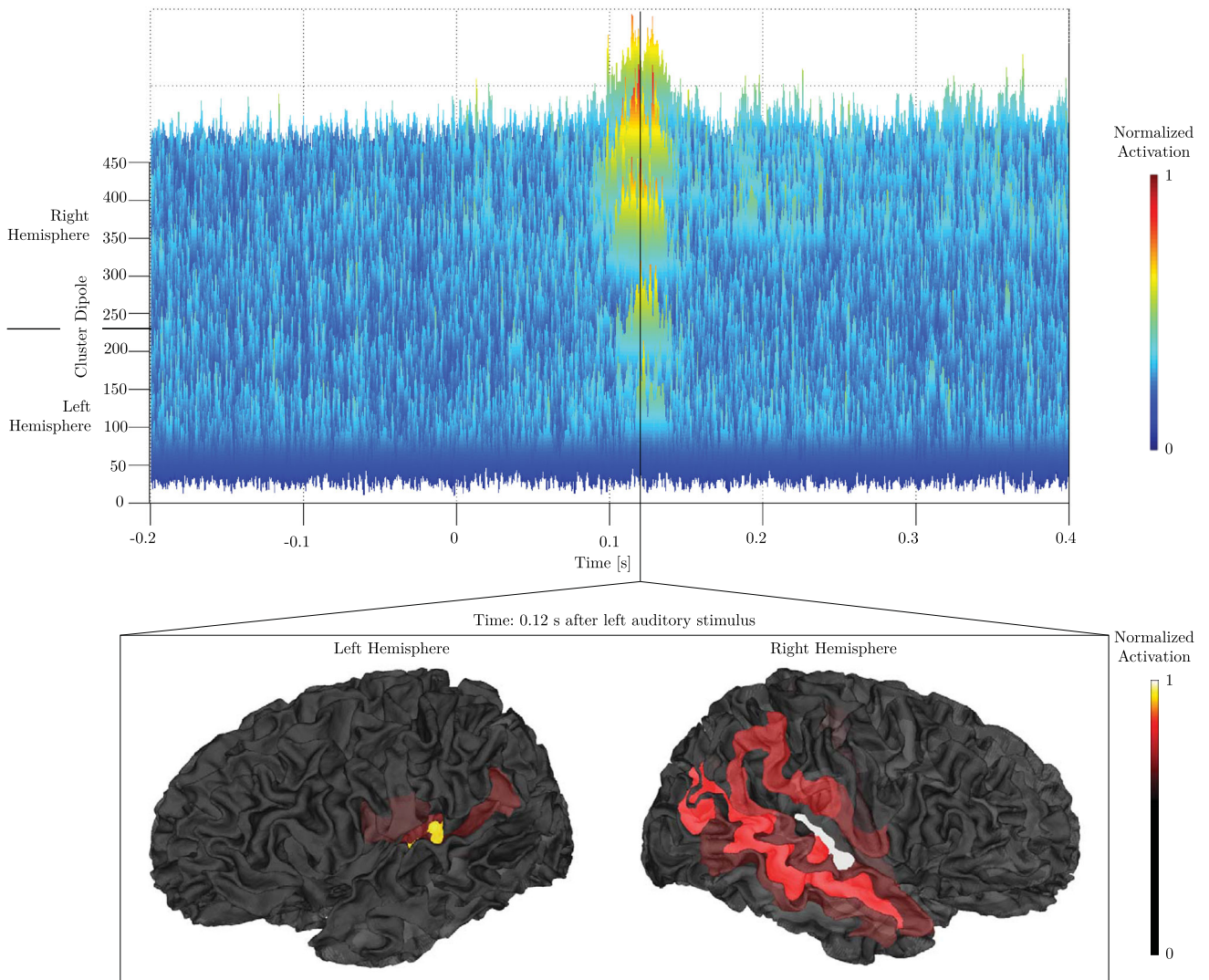

Fig. 14 N100 dSPM localization result of a left auditory stimulus using 10 averages. The upper part visualizes the cluster activation of all clusters over time. The corresponding topography on the white matter surface for the time point 12 s after the stimulus is shown at the bottom

to verify that localization results of the MNE can be provided in real-time. Sampling rates up to 1250 Hz and a clustered gain matrix mapping 416 regions to 306 MEG sensors were handled by the processing chain. The internal sample buffer of the MEG device had a minimal size of at least 28 samples. That led to an average delay of 11.2 ms given a sampling rate of 1250 Hz. The computation of MNE for all samples within a 10 ms window took only 3.36 ± 0.97 ms and was, therefore, faster than the delay of the MEG system, which allowed to follow the data stream in real-time. This caused an overall average delay of approximately 15 ms, when the inverse calculation was directly applied to the real-time data stream.

Discussion

Real-time source localization involves two major challenges: low SNR and the limited time available for the computations. We addressed both issues by reducing the gain matrix. The computational cost was thus reduced and at the same time sources were easier to distinguish in the presence of noise, i.e., the inverse problem was better conditioned, and the crosstalk as well as the point spread were reduced.

We compared seven different reduction methods, see Table 1, and the original dense gain matrix. The results in Sect. 3.1 show that all gain matrix clustering methods led to a significant reduced crosstalk compared to selecting a fewer amount of dipoles or the original dense gain matrix. The point spread was reduced compared to method III_{L_1} and the original dense gain matrix. In contrast to simple selection, the proposed clustering approach I_{L_1} ensures that the reduced sampling of the source space is spatially and anatomically representative for the respective region.

Method I_{L_1} reduces the gain matrix by calculating representative dipoles per parcellation, increasing the ability to distinguish regions even in the presence of a low SNR, which is indicated by the better condition (Fig. 8). This method had the lowest computational cost, showed a significant improved crosstalk compared to the selection method (IV) and the point spread performed similarly. Thus it was selected for the further examinations. The inverse calculation was applied to a reduced number of dipoles at the same time and could therefore be performed with ordinary workstations in real-time.

However, both real-time challenges were met at the cost of the resolution in space and sensitivity. First, only regions could be localized. Second, the k-means algorithm reduced the spread between the dipoles of the clustered gain matrix G^*, increasing the condition κ of the clustered gain matrix G^* and therewith the ill-

posedness of the inverse problem. This effect was even more prominent when the L_2-norm was applied, whereas the L_1-norm helped to preserve a stronger separation between the cluster centers.

The number of centroids per region was determined by the cluster size and was also evaluated. A large cluster size is favorable in terms of computation cost, but on the other hand possibly averages out dipole diversity. We determined the size by evaluating the condition for different cluster sizes (Fig. 8) from a full gain matrix with approximately 7500 dipoles. Also, taking into account the calculation speed, a cluster size containing 20 dipoles was favored.

The presented method showed a high localization precision when applied to raw data streams. Auditory responses on the cortex were localized with small error using averages of only four trials. The activation was correctly localized at and around the superior temporal gyrus. The comparison to a dipole reference localization was successful and showed good performance.

Since Wehner et al. (2008) found that source localization is relatively robust towards movement of the head, we did not apply a head movement correction in the real-time processing chain. However, an increase of the localization accuracy can be expected when head movement correction is applied. We are currently developing strategies of head movement corrections in the related BabyMEG project (Papadelis et al. 2013), which we will apply in future.

The results showed that the clustering performs well using the k-means algorithm. However, we are aware of the limits of k-means, i.e., dependency of the initialization, number of clusters must be known and the convex nature of the clusters. In future work, we will investigate further clustering algorithms, e.g., density-based spatial clustering of applications with noise (DBSCAN).

Babadi et al. (2014) recently proposed a clustering technique which uses the most significant eigenmodes of pre-computed Voronoi regions. In comparison to that, we used an anatomical brain atlas instead of Voronoi regions which allows to keep an anatomical, often related to a functional, representation of the cortex and provides an easily interpretable result for our real-time monitor. Furthermore, by calculating clusters using k-means we were able to cluster a free orientated gain matrix and were still able to calculate a reduced gain matrix. Another gain matrix clustering method was introduced by Chowdhury et al. (2013), which determines the clusters on a pre-localization basis and is therefore data driven. Here we propose a model-driven clustering which is based on the electromagnetic characteristics of the gain matrix. This allows us to conduct real-time localization without knowing the source estimates in advance.

Conclusion

We demonstrated that the selected real-time source localization approach can correctly locate sources of stimulus-locked activity in real-time. We showed that the source localization results can be calculated almost in real-time with an average delay of approximately 16 ms up to a sampling frequency of 1250 Hz for 306-channel MEG data. We anticipate that the presented approach is suitable for several scenarios, e.g., the visualization and monitoring of ongoing activity to give a real-time feedback, to refine the localization within the most active regions followed by a subsequent high-resolution source localization, and to increase the accuracy of BCIs based on regional brain activity estimates.

Conflict of interest The authors declare that they have no conflict of interest.

Ethical Approval All procedures performed in studies involving human participants were in accordance with the ethical standards of the institutional and/or national research committee and with the 1964 Helsinki declaration and its later amendments or comparable ethical standards.

Informed Consent Informed consent was obtained from all individual participants included in the study. Additional informed consent was obtained from all individual participants for whom identifying information is included in this article.

References

Babadi B, Obregon-Henao G, Lamus C, Hamalainen MS, Brown EN, Purdon PL (2014) A subspace pursuit-based iterative greedy hierarchical solution to the neuromagnetic inverse problem. NeuroImage 87:427–443. doi:10.1016/j.neuroimage.2013.09.008

Besserve M, Martinerie J, Garnero L (2011) Improving quantification of functional networks with EEG inverse problem: evidence from a decoding point of view. NeuroImage 55(4):1536–1547. doi:10.1016/j.neuroimage.2011.01.056

Chowdhury RA, Lina JM, Kobayashi E, Grova C (2013) MEG source localization of spatially extended generators of epileptic activity: comparing entropic and hierarchical Bayesian approaches. PLOS One 8(2):e55,969. doi:10.1371/journal.pone.0055969

Dale AM, Liu AK, Fischl B, Buckner RL, Belliveau JW, Lewine JD, Halgren E (2000) Dynamic statistical parametric mapping: combining fMRI and MEG for high-resolution imaging of cortical activity. Neuron 26(1):55–67. doi:10.1016/S0896-6273(00)81138-1

Destrieux CE, Fischl B, Dale A, Halgren E (2010) Automatic parcellation of human cortical gyri and sulci using standard anatomical nomenclature. NeuroImage 53(1):1–15. doi:10.1016/j.neuroimage.2010.06.010

Digia Plc: Qt 5.3. http://qt-project.org/ (1991–2014)

Dinh C, Luessi M, Sun L, Haueisen J, Hamalainen MS (2013) MNE-X: MEG/EEG real-time acquisition, real-time processing, and real-time source localization framework. Biomed Eng 58(1):4184. doi:10.1515/bmt-2013-4184

Dinh C, Strohmeier D, Haueisen J, Güllmar D (2012) Brain atlas based region of interest selection for real-time source localization using k-means lead field clustering and RAP-MUSIC. Biomed Eng 57(Suppl 1):813. doi:10.1515/bmt-2012-4316

Eichardt R, Baumgarten D, Petković B, Wiekhorst F, Trahms L, Haueisen J (2012) Adapting source grid parameters to improve the condition of the magnetostatic linear inverse problem of estimating nanoparticle distributions. Med Biol Eng Comput 50(10):1081–1089. doi:10.1007/s11517-012-0950-4

Fischl B (2012) FreeSurfer. NeuroImage 62(2):774–781. doi:10.1016/j.neuroimage.2012.01.021

Friedman M (1937) The use of ranks to avoid the assumption of normality implicit in the analysis of variance. J Am Stat Assoc 32:675–701. doi:10.1080/01621459.1937.10503522

Gramfort A, Luessi M, Larson E, Engemann DA, Strohmeier D, Brodbeck CM, Parkkonen L, Hamalainen MS (2013) MNE software for processing MEG and EEG data. NeuroImage. doi:10.1016/j.neuroimage.2013.10.027

Hamalainen MS, Hari R, Ilmoniemi RJ, Knuutila J, Lounasmaa OV (1993) Magnetoencephalography-theory, instrumentation, and applications to noninvasive studies of the working human brain. Rev Mod Phys 65(2):413–497. doi:10.1103/RevModPhys.65.413

Hamalainen MS, Ilmoniemi RJ (1994) Interpreting magnetic fields of the brain: minimum norm estimates. Med Biol Eng Comput 32(1):35–42. doi:10.1007/BF02512476

Jones SR, Kerr CE, Wan Q, Pritchett DL, Hamalainen MS, Moore CI (2010) Cued spatial attention drives functionally relevant modulation of the mu rhythm in primary somatosensory cortex. J Neurosci 30(41):13,760–13,765. doi:10.1523/JNEUROSCI.2969-10.2010

Lin FH, Witzel T, Ahlfors SP, Stufflebeam SM, Belliveau JW, Hämäläinen MS (2006) Assessing and improving the spatial accuracy in MEG source localization by depth-weighted minimum-norm estimates. NeuroImage 31(1):160–71. doi:10.1016/j.neuroimage.2005.11.054

Lloyd SP (1982) Least squares quantization in PCM. IEEE Trans Inf Theory 28(2):129–137. doi:10.1109/TIT.1982.1056489

Mann HB, Whitney DR (1947) On a test of whether one of two random variables is stochastically larger than the other. Ann Math Stat 18(1):50–60. doi:10.1214/aoms/1177730491

Michel CM, Pascual-Marqui RD, Strik WK, Koenig T, Lehmann D (1995) Frequency domain source localization shows state-dependent diazepam effects in 47-channel EEG. J Neural Trans Gen Sect 99(1–3):157–171. doi:10.1007/BF01271476

Ou W, Golland P, Hamalainen MS (2007) Sources of variability in MEG. Med Image Comput Comput Assist Interv 10(Pt 2):751–759. doi:10.1007/978-3-540-75759-7-91

Papadelis C, Harini C, Ahtam B, Doshi C, Grant E, Okada Y (2013) Current and emerging potential for magnetoencephalography in pediatric epilepsy. J Pediatr Epilepsy 2(1):73–85

Soekadar S, Birbaumer N, Cohen L (2011) Brain-computer-interfaces in the rehabilitation of stroke and neurotrauma. In: Kenji K, Cohen LG (eds) Systems Neuroscience Rehabilitation. Springer, Japan, pp 3–18. doi:10.1007/978-4-431-54008-3-1

Sudre G, Parkkonen L, Bock E, Baillet S, Wang W, Weber DJ (2011) rtMEG: a real-time software interface for magnetoencephalography. Comput Intell Neurosci 2011:327,953. doi:10.1155/2011/327953

Supek S, Aine CJ (1993) Simulation studies of multiple dipole neuromagnetic source localization: model order and limits of source resolution. IEEE Trans Bio Med Eng 40(6):529–540. doi:10.1109/10.237672

Tarkiainen A, Liljeström M, Seppä M, Salmelin R (2003) The 3D topography of MEG source localization accuracy: effects of conductor model and noise. Clin Neurophys 114(10):1977–1992. doi:10.1016/S1388-2457(03)00195-0

Wehner DT, Hämäläinen MS, Mody M, Ahlfors SP (2008) Head movements of children in MEG: quantification, effects on source estimation, and compensation. NeuroImage 40(2):541–50. doi:10.1016/j.neuroimage.2007.12.026

Weisend M, Hanlon F, Montaño R, Ahlfors SP, Leuthold A, Pantazis D, Mosher JC, Georgopoulos A, Hämäläinen MS, Aine C (2007) Paving the way for cross-site pooling of magnetoencephalography (MEG) data. Int Congr Ser 1300:615–618. doi:10.1016/j.ics.2006.12.095

Wilcoxon F (1945) Individual Comparisons by ranking methods. Biom Bull 1(6):80–83

Ziegler DA, Pritchett DL, Hosseini-Varnamkhasti P, Corkin S, Hamalainen MS, Moore CI, Jones SR (2010) Transformations in oscillatory activity and evoked responses in primary somatosensory cortex in middle age: A combined computational neural modeling and MEG study. NeuroImage 52(3):897–912. doi:10.1016/j.neuroimage.2010.02.004